Jet Mixing Noise from Single Stream Jets using Stochastic Source Modeling

A. Neifeld* and R. Ewert†

Institute of Aerodynamics and Flow Technology, Technical Acoustics Branch,

German Aerospace Center (DLR), Lilienthalplatz 7, 38108 Braunschweig, Germany

This work deals with the simulation of jet mixing noise in the time domain using stochastic source modeling. The sound sources are generated by means of the RPM (*R*andom *P*article *M*esh) method, which uses turbulence statistics gained from RANS data. The generated stochastic sound sources closely realize the two-point cross-correlation function proposed by Tam & Auriault (T&A) to describe the statistics of a fine-scale jet mixing noise source. By modeling the sound source in the time domain a direct (primal) prediction method of the T&A approach is realized. The methodology followed in this work allows to evaluate noise spectra at any position in the computational domain based on one CAA computation. The aspired goal is to prove numerically the ability of our time-domain model to give similar predictions as the genuine T&A approach. The realization of an eight power Mach number scaling law for the emitted sound is verified. Furthermore, it is demonstrated that jet similarity spectra are obtained with a time marching CAA code. At 90° to the jet axis good agreement with the G-Spectrum is found. The stochastic approach is slightly modified to enable Strouhal similarity for the peak level of the jet-noise spectra at different jet velocities. The appropriate scaling behavior is demonstrated numerically. The spectra are realized in a Mach number range between 0.3 and 0.9 for Strouhal numbers ranging from 0.01 to 10. The RANS solution to a single stream cold jet configuration is obtained for a set of subsonic Mach numbers using the DLR solver TAU.

I. Introduction

During the last two decades reasonable achivements in numerical jet noise computations have been achieved. Especially in the domain of high fidelity sound computations (DNS, LES or DES) big efforts are done to predict with highest accuracy the emitted sound of a jet. But at the moment, there is a lack of time efficient methods for jet noise prediction, which would be of interest for design purposes. With the approach of stochastic source modeling this goal can be well reached, since it is able to cover relatively big acoustic source domains with a managable computational effort. Nevertheless, the prediction of the sound spectra is expected to contain some of the relevant physical phenomena with sufficient accuracy. The intention here is not to resolve the smallest scales of the turbulence, but to describe the characteristic sound emissions of turbulence.

This paper has the following structure: In Sec. II the realized acoustical source model based on the Random Particle-Mesh (RPM) method is described. The discretization of the sources starting from statistical RANS data, the filter kernel of RPM and its weighting with the white noise are briefly discussed. In Sec. III the computational parameters and required computational time of CFD and CAA simulations are described. The Sec. IV deals about the cases conducted as two-dimensional computations. High frequency excess noise emitted from the region next to the nozzle trailing edge is observed. This phenomenon was found in computations, where the grid resolution was sufficiently high, i.e. $Str = 10$ to resolve the frequency of the excess noise. Subsequently, results of 3-D modal computations are presented. The 3-D modal computations were conducted with a grid resolution for a Strouhal number up to $Str = 2$. The Mach scaling law, which is predicted by measurements and also by T&A source term as Ma^8-law for jet noise is discussed. The

*Research Scientist, AIAA Member

†Research Scientist, Senior Member AIAA

scaling is studied for 2-D as well as for 3-D modal computations. The effect of boundary layer thickness at the nozzle trailing edge on the emitted sound and its directional characteristics is discussed. The thickness of the boundary layer is influenced by the length of the circular duct. In Sec. V the extension of the code to the 3-D modal computations is described. The implementation and the verification cases are closely described. The test cases with circular and annular ducts are used to verify the implemented equations with the analytical solutions. The results of jet noise compuations with Mach variation and azimuthal mode computations for $m = 1 \ldots 5$ are shown. In Sec. VI the mean flow gradients in the governing linearized Euler equations (LEE) are included, whose inclusion trigger large scale noise in the computations. In previous sections by omitting these terms only the fine scale noise was considered.

II. Numerical Approach of RPM

A. Acoustic Model

A scalar source term is realized stochastically, which appears on the right-hand side of the pressure equation of the linearized Euler equations (LEE),

$$\begin{aligned} \rho_0 \left[\tfrac{\partial u'}{\partial t} + u_0 \nabla u' \right] + \nabla p &= 0 \\ \tfrac{\partial p}{\partial t} + u_0 \nabla p + \gamma p_0 \nabla \cdot u' &= q_p. \end{aligned} \tag{1}$$

The acoustical sources are realized with the RPM method.[5] If the fluctuating source term is identified with the fine-scale source term of Tam & Auriault,[2] i.e.

$$q_p \equiv \frac{Dq_s}{Dt}, \tag{2}$$

the noise prediction model is formally identical with that used in Tam & Auriault,[2] providing the fluctuations have cross-correlations following the model

$$\left\langle \left(\frac{Dq_s}{Dt} \right)_1 \left(\frac{Dq_s}{Dt} \right)_2 \right\rangle = \hat{R} \times \exp \left\{ -\frac{|\xi|}{u_j \tau_s} - \frac{ln2}{l_s^2} [(\xi - u_j \tau)^2 + \eta^2 + \zeta^2] \right\}, \tag{3}$$

where

$$\hat{R} = \frac{\hat{q}_s^2}{c^2 \tau_s^2}. \tag{4}$$

The variables ξ, η, and ζ denote the relative distance between position 1 and position 2, u_j indicates the jet convection velocity, and τ_s and l_s indicate a time- and length-scale, respectively. The variance $\hat{R}$ is entirely specified by a RANS solution utilizing a two-equation turbulence model.

The fluctuating component q_p is obtained convolving of spatiotemporal convective white-noise $\mathcal{U}$ with a filter kernel,

$$q_p = \int_{V_S^n} \hat{A} G \left(\boldsymbol{x} - \boldsymbol{x}' \right) \mathcal{U} \left(\boldsymbol{x}', t \right) \mathrm{d}^n x'. \tag{5}$$

In this expression G is a Gaussian filter kernel, n indicates the dimension of the problem, and V_S^n is the considered source region. The scaling function $\hat{A}$ realizes the desired variance of q_p. Here it is assumed to be a function of $\boldsymbol{x}'$. The convective white-noise is specified by

$$\langle \mathcal{U}(\boldsymbol{x}, t) \rangle = 0 \tag{6}$$

$$\langle \mathcal{U}(\boldsymbol{x}, t) \mathcal{U}_j(\boldsymbol{x} + \boldsymbol{r}, t) \rangle = \rho_0(\boldsymbol{x})^{-1} \delta(\boldsymbol{r}) \tag{7}$$

$$\frac{D_0}{Dt} \mathcal{U} = -\frac{1}{\tau_s} \mathcal{U} + \sqrt{\frac{2}{\tau_s}} \mathcal{V}, \tag{8}$$

where $\mathcal{V}$ is an additional spatio-temporal white-noise source[7] and $\frac{D_0}{Dt} := \frac{\partial}{\partial t} + \vec{u_0} \cdot \nabla$. Based on this model, it can be shown analytically that the generated unsteady source exhibits a cross-correlation of the form

$$\langle q_p(\boldsymbol{x}, t) q_p(\boldsymbol{x} + \boldsymbol{r}, t + \tau) \rangle = \hat{R} \times \exp \left\{ -\frac{|\tau|}{\tau_s} - \frac{\ln(2)}{l_s^2} \left[(\xi - u_j \tau)^2 + \eta^2 + \zeta^2 \right] \right\}. \tag{9}$$

if a scaling

$$\hat{A} = \left(\frac{4\ln(2)}{\pi}\right)^{\frac{n}{4}} \sqrt{\frac{\rho_0 \hat{R}}{l_s^n}} \tag{10}$$

is applied together with $\vec{u}_0 = (u_j, 0, 0)^T$. The density is specified by $\nabla \cdot (\rho_0 \vec{u}_0) = 0$. If a constant convection $\vec{u}_0 = (u_j, 0, 0)^T$ is applied, ρ_0 is a constant. The length scale, time scale, and source variance are directly derived from the RANS solution. For example, the length scale is obtained from

$$l_s = \frac{c_l}{C_\mu} \frac{k^{1/2}}{\omega}, \tag{11}$$

with $c_l = 0.273$ and $C_\mu = 0.09$. Two differences to the genuine cross-correlation model used by Tam & Auriault Eq. (3) appear in the cross-correlation formulation Eq. (9). Firstly, ξ/u_j is substituted for $|\tau|$ in the exponential function. If the auto-correlation is evaluated as a function of time delay τ the Tam & Auriault model gives a Gaussian shape with a relatively large curvature at the origin (i.e. a large Taylor length scale), whereas Eq. (9) exhibits a sharp peak at $\tau = 0$, resulting in a shape, which is closer to the experimentally observed velocity correlations.

Note that the RPM generated fluctuations approximately satisfy Taylor's convection hypothesis, which allows to substitute $|\tau|$ for ξ/u_j in the Tam & Auriault model and thus the cross-correlations would be equal to Eq. (9). However, strictly speaking, the two-point correlations do not describe frozen turbulence since they include a temporal decorrelation mechanism. Hence, the cross-correlation used in the Tam & Auriault model and Eq. (9) are not exactly equivalent. The differences will be discussed in detail in Sec. IV. The cross-correlation model Eq. (9) was used also by Morris & Boluriaan[11] to simulate jet noise.

B. RPM Discretization

In the RPM discretization the integral Eq. (5) is replaced by a discrete sum over random particles. It was shown in Ref. of Ewert et al.[7] that the particle approach yields a consistent discretization of the analytical model.

To each particle a random variable r_k is associated. The source is generated through the weighted sum over all N particles, summing up the random variates associated to the source, i.e.

$$q_p(\boldsymbol{x}, t) \simeq \sum_{k=1}^{N} G\hat{A}(\boldsymbol{x}') \ (\boldsymbol{x} - \boldsymbol{x}_k^c(t)) \frac{r_k(t)}{\rho_0(\boldsymbol{x}_k^c)}. \tag{12}$$

The function $\hat{A}$ specifies the variance of the fluctuations realized. It can be a given as a function of either in particle or mesh coordinates, i.e. $\hat{A}(\boldsymbol{x}')$ or $\hat{A}(\boldsymbol{x})$, respectively. In this work a Gaussian filter kernel is applied for G. Each particle represents the aforementioned convective white-noise field over a representative control volume surrounding each particle. The random variables satisfy the conditions

$$\langle r_k(t) \rangle = 0 \tag{13}$$

$$\langle r_k(t) r_l(t) \rangle = \delta_{kl} \delta m_k \tag{14}$$

$$\dot{r}_k = -\frac{1}{\tau_s} r_k + \sqrt{\frac{2}{\tau_s}} s_k \tag{15}$$

$$\dot{\boldsymbol{x}}_k^c = \boldsymbol{u}_j(\boldsymbol{x}_k^c). \tag{16}$$

In plain words, the random variables r_k have vanishing mean and a constant variance proportional to δm_k, which is the fluid mass encompassed by the control volume surrounding each particle. The particle drift with the local mean flow velocity at the particle position $\boldsymbol{x}_k^c$. The random values are generated with a Langevin equation, Eq. (16), which realizes the exponential time decorrelation.

In the RPM discretization a bundle of mean-flow streamlines covers the resolved source domain. Starting from a seeding rake in an upstream position, equidistant streamlines are generated and truncated at a desired downstream position. The width and length of this source patch defines the region where stochastic sound sources are generated.

Random particles are seeded with a constant clock rate at the foremost upstream position on each streamline. The particles drift along the streamline until being finally removed downstream. The mean-flow

of RANS is taken to prescribe this source convection. The spatial filtering is conducted sequentially. Due to the properties of a Gaussian filter, the discrete filtering Eq. (12) can be split into a sequence of 1-D operations along orthogonal coordinate directions. In the first step the random values are filtered along the streamline. Next, the values are weighted and distributed in direction normal to the streamline onto the CAA mesh. The streamlines usually exhibit a slight curvature such that the sequence of 1-D discrete filtering steps occurs not exactly along orthogonal coordinate directions. The related error is usually negligible.

C. Numerical source statistics

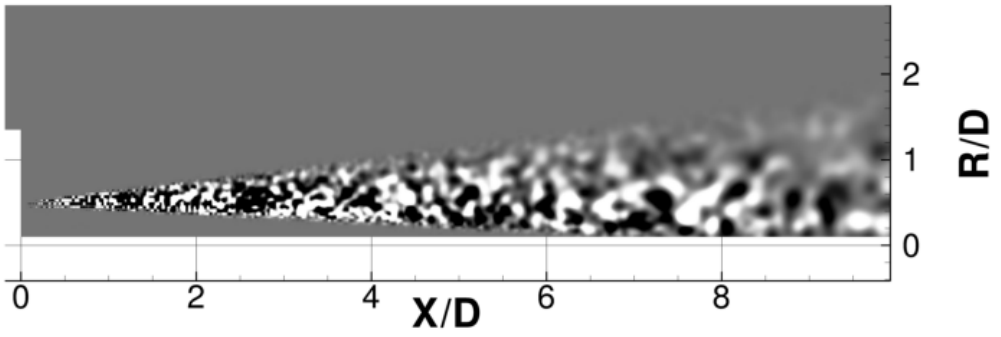

(a)

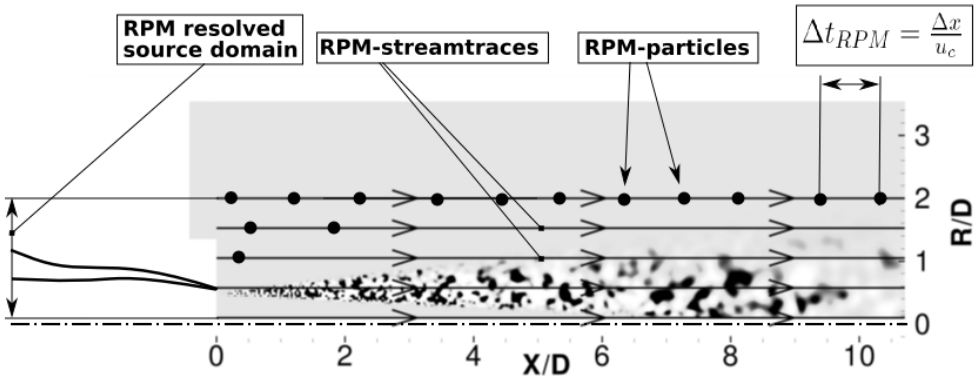

(b)

Figure 1. (a) RPM source distribution in the shear layer of a jet; (b) Significant parameters of RPM

To ascertain, the source correlation is correctly applied, we conducted a comparison between theoretically expected correlation and effectively generated correlation in the CAA domain. In this comparison we found well matching spatial-correlations in the vicinity of the reference position and reasonable good agreement in the cross-correlation, which is depicted in Fig. 2. The expected correlation describes the exponential term in (3).

Fig. 2(b) presents cross-correlations of different microphones (i.e. sampling positions) pairs over time off-set τ_s. The distance increment between the microphones is $\Delta x = 0.1$. In total 8 microphones are used for this study. The effect of time decorrelation is highlighted, showing an exponential reduction of the peak correlation values with growing distance between virtual microphones. This decorrelation contributes reasonably to the jet noise generation. The temporal decay of evolving turbulence is accomplished by a first-order Langevin equation (17), to compute the random variance of each particle. That means, the particles carrying random values, variate that value over time, according to the discrete Langevin equation.

$$r_i^{n+1} = \alpha r_i^n + \beta s_i^n \quad \text{with} \quad \beta = \sqrt{1-\alpha^2} \tag{17}$$

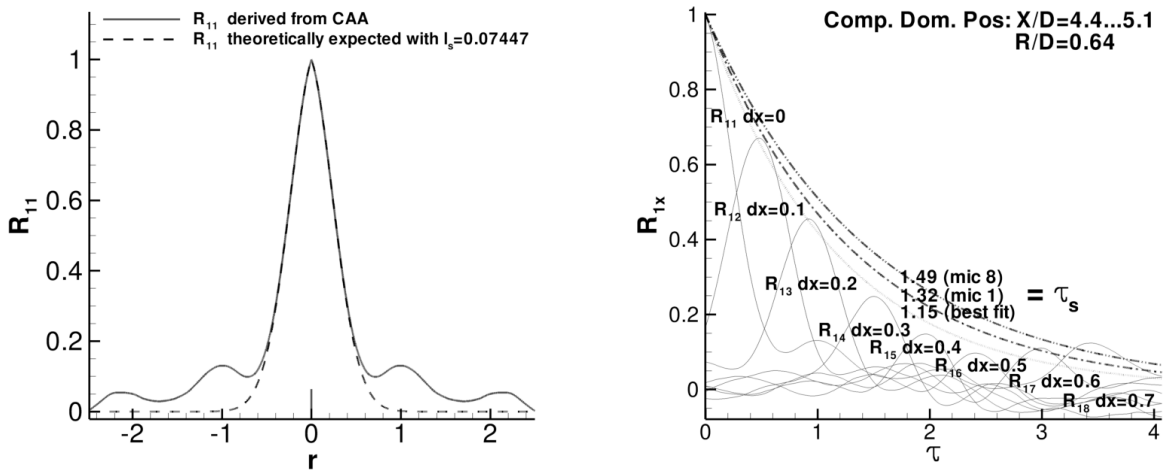

Figure 2. Correlations within the source domain: (a) Spatial-correlation; (b) Cross-correlation

Here, r and s are two different random values, and α and β are decorrelation coefficients that follow from the numerical realization of Eq. (15).

III. Computational Setup

A. CFD settings

A set of jet RANS solutions for different subsonic Mach numbers $(0.3, 0.5, 0.6, 0.7, 0.75, 0.8,\ 0.9, 0.95)$ were processed, covering Reynolds numbers in a range between $1.0 \cdot 10^6 ... 20 \cdot 10^6$. Variations in nozzle geometry (double convergent and pipe nozzle) were conducted in conjunction with the choice of different nozzle diameters, the latter of which has a reasonable influence on the boundary layer thickness at the nozzle lip. Since we considered in this work axisymmetric single-stream jets, a segment (30°) of the jet was resolved in the computations. The extensions of the computational domain was 50 jet diameters in downstream direction and 15 jet diameters in radial direction. The jet diameter varied between 0.05 m and 1.0 m. The structured grids had roughly around one million points depending on the actual considered geometry. The ambient temperature and density were chosen as $T_\infty = 288.15$ K and $\rho_\infty = 1.225\ \frac{\text{kg}}{\text{m}^3}$. For all these computations a standard Menter-SST turbulence model was applied. Each computation was conducted within 48 hours real time in parallel mode on $32 - 96$ CPUs.

B. CAA settings

The RPM source module is applied in combination with the DLR CAA solver PIANO (*P*erturbation *I*nvestigation of *A*erodynamic *N*oise). To resolve frequencies up to Strouhal number of 10, there was a need for $0.95 \cdot 10^6$ points for the 2-D CAA grid. The grids used in the modal computations have seven 2-D planes in the imaginary and in the real domain i.e. 14 planes each with $1.6 \cdot 10^5$ points ($2.24 \cdot 10^6$ points), which are able to resolve a maximum Strouhal number of $Str = 2.0$. The highest refinement occurred next to the nozzle, subsequently following the spreading rate and becoming coarser further downstream. The extension of the CAA domain is 15 jet diameter in radial direction and 30 jet diameter in downstream direction. The RPM source domain encloses a region of $R/D = 0.1...2$ and $X/D = 0...30$. In the source domain 50 streamlines prescribe the particle traces used for the RPM modell. The number of particles on each streamline is of the order of 10^3. The exact value depends on the convection velocity on the streamline. To adopt the original Tam & Auriault approach,[2] a constant convection velocity parallel to the jet axis is considered. Each computation was conducted in $48 - 96$ hours real time in parallel mode on 8 CPUs depending on the targeted sample time. The non-dimensional numerical time step is 0.0015 in 2-D and 0.001 in modal

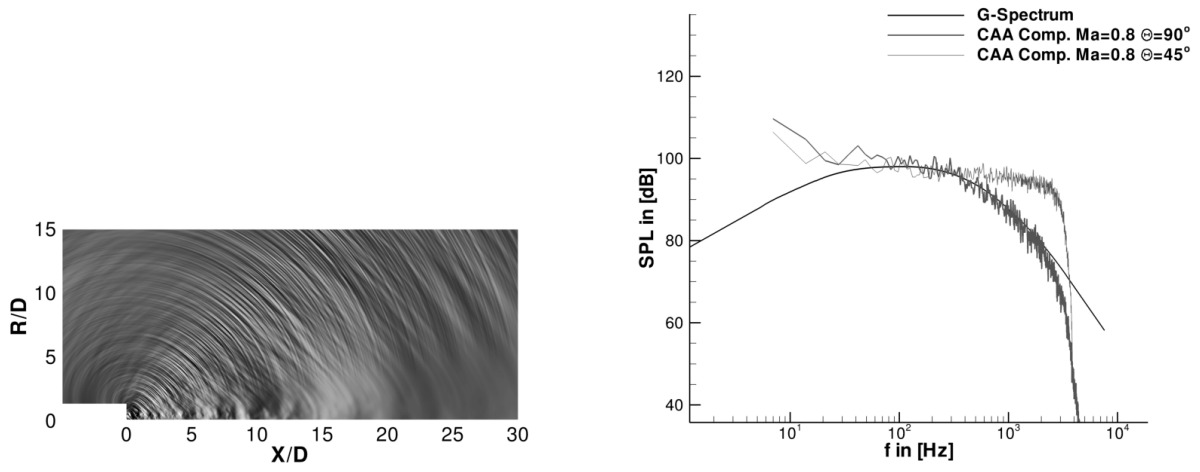

(a) (b)

Figure 3. PIANO computation for a double convergent nozzle $Ma = 0.8$: (a) Sound pressure field; (b) Spectra at $\theta = 45°$ and at $\theta = 90°$

computations, which is prescribed by the smallest grid spacing. This correspond to a physical time step of $2.2 \cdot 10^{-6}$sec and $1.5 \cdot 10^{-6}$sec respectively. The seeding rate of particles was chosen as non-dimensional frequency of $8.3\overline{3}$ for a jet with $Ma = 0.8$. This frequency is the upper bound of frequency resolution (Nyquist condition) and should be bigger than grid frequency resolution. With these parameters we were able to simulate jet noise samples of 2.34 seconds real time duration. All these acoustic simulations are governed by the linearized Euler equations formulated in cartesian as well as in cylindrical coordinates for the modal computations. The spatial discretization uses the dispersion relation preserving seven point stencil finite difference scheme (Tam&Webb[1]) on curvilinear structered grids. For the temporal discretization a fourth order low-dissipation, low-dispersion Runge-Kutta scheme is used.

IV. 2-D jet noise computations

A. Strouhal and Helmholtz similarity

First, we have studied the acoustic differences between the cross-correlation model used and the genuine Tam & Auriault cross-correlation model. To summarize, the Tam & Auriault model reads

$$\left\langle \frac{D_0 q_{s1}}{Dt_1} \frac{D_0 q_{s2}}{Dt_2} \right\rangle = \frac{\hat{q}_s^2}{c^2 \tau_s^2} \times \exp\left\{ \boxed{-\frac{|\xi|}{u_j \tau_s}} - \frac{ln2}{\hat{l}_s^2}[(\xi - u_j\tau)^2 + \eta^2 + \zeta^2] \right\}, \tag{18}$$

whereas the RPM cross-correlation model corresponds to that used by Morris & Boluriaan,[11] which reads

$$\left\langle \frac{D_0 q_{s1}}{Dt_1} \frac{D_0 q_{s2}}{Dt_2} \right\rangle = \frac{\hat{q}_s^2}{c^2 \tau_s^2} \times \exp\left\{ \boxed{-\frac{|\tau|}{\tau_s}} - \frac{ln2}{\hat{l}_s^2}[(\xi - u_j\tau)^2 + \eta^2 + \zeta^2] \right\}. \tag{19}$$

The terms in the boxes represent in principle the same expression, assuming validity of the Taylor hypothesis $\xi = u_j\tau$. However, the analytical derived spectra show a significant discrepancy.

The spectrum generated by the genuine Tam & Auriault model becomes

$$\hat{S}(\vec{x}, \omega) = \left(\frac{\pi}{\ln(2)} \right)^{3/2} \int_{V_s} \frac{\hat{q}_s^2 l_s^3}{c^2 \tau_s} |\hat{p}_a(\vec{x}_1, \vec{x}, \omega)|^2 \frac{\boxed{\exp\left[-\frac{\omega^2 l_s^2}{4\ln(2) u_j^2} \right]}}{1 + \omega^2 \tau_s^2 (1 - M_0 \cos\theta)^2} \mathrm{d}\vec{x}_1 \tag{20}$$

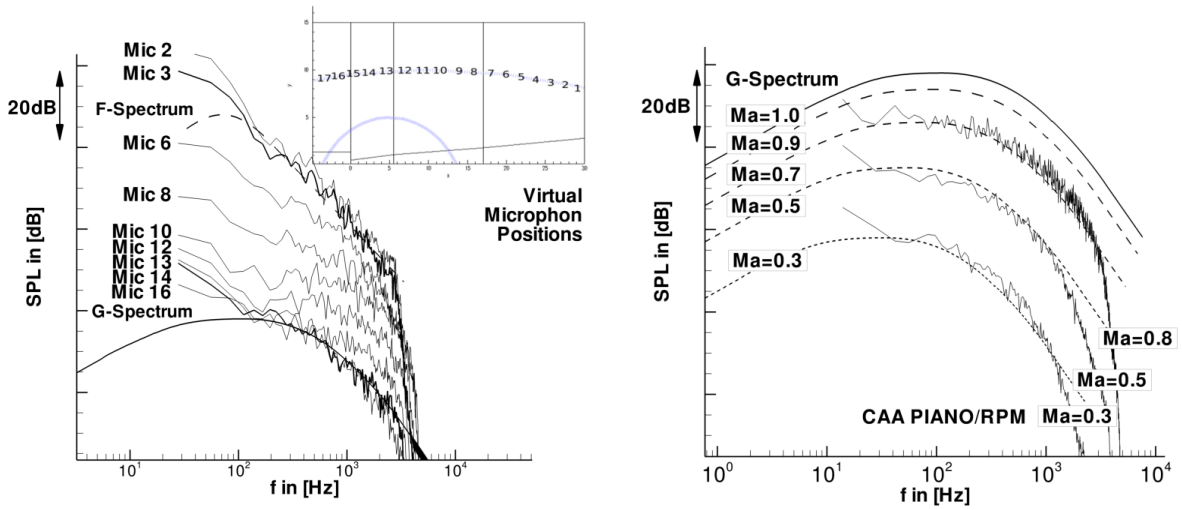

Figure 4. CAA spectra (resolution: $Str = 10$) versus G-Spectrum and F-Spectrum: (a) Spectra at different angles for computation with mean flow gradients, spectra vertically shifted (double convergent nozzle, $Ma = 0.8$); (b) PIANO spectra for $Ma = 0.3, 0.5, 0.8$ in comparison with G-Spectra (Strouhal similarity correction applied)

The spectrum generated by RPM cross-correlation model becomes

$$\hat{S}(\vec{x},\omega) = \left(\frac{\pi}{\ln(2)}\right)^{3/2} \int_{V_s} \frac{\hat{q}_s^2 l_s^3}{c^2 \tau_s} |\hat{p}_a(\vec{x}_1,\vec{x},\omega)|^2 \frac{\boxed{\exp\left[-\frac{\omega^2 l_s^2}{4\ln(2)c_0^2}\right]}}{1+\omega^2\tau_s^2(1-M_0\cos\theta)^2} \mathrm{d}\vec{x}_1 \tag{21}$$

For the derivation of these spectra refer to Ewert et al.[8] and Tam et al.[2] In these expressions $\hat{p}_a$ denotes the Green's function of the problem. To subsume, the cross-correlation models have a subtle but distinct effect on the spectra,[11] i.e. the argument of the exponential function changes from $-\frac{\omega^2 l_s^2}{4\ln(2)u_j^2}$ in Eqn. (20) to $-\frac{\omega^2 l_s^2}{4\ln(2)c_0^2}$ in Eqn. (21). Since the exponential function controls the roll-off of the spectra, Helmholtz similarity $He = \frac{\omega l_s}{c_0}$ are obtained with the cross-correlation model Eq. (19), while the Tam & Auriault source model Eq. (18) yields Strouhal similarity $Str = \frac{\omega l_s}{u_j}$. To correct this deviation, we found that it is valid to use a modified length scale coefficient c_l to transform the spectra to Strouhal similarity. By using the scaling $c_l^* = \frac{c_l}{Ma}$ in Eqn. (11) a modified length scale $l_s^* = \frac{l_s}{Ma}$ follows, that in conjunction with the spectrum from Eqn. (21) yields an argument - $\frac{\omega^2 l_s^2}{4\ln(2)c_0^2} = -\frac{\omega^2 l_s^2}{4\ln(2)u_j^2}$, i.e. Strouhal similarity. However, the variance is affected by this correction as well, which can be neutralized by multiplying it with the Ma^n (n is spatial dimension of the computation). Altoghether the scaling becomes

$$c_l^* = \frac{c_l}{Ma} \qquad \hat{R}^* = \hat{R} \cdot Ma^n \qquad \text{with} \qquad c_l = 0.256 \tag{22}$$

After this correction, the spectra, ploted over frequency, show the desired frequency dependency in respect to chosen Mach number (refer to Fig. 4(b)).

B. High frequency excess noise

After evaluation of spectra for different observer angles with respect to the nozzle exit, we found a quite good agreement with the G-Spectrum for radiation directions around $\theta = 90°$. However, there is a noticeable directional dependency in our computations, showing deviation of higher frequencies in amplitude peaking at $\theta = 45°$. This high frequency radiation can readily be seen in the sound pressure field, which is shown

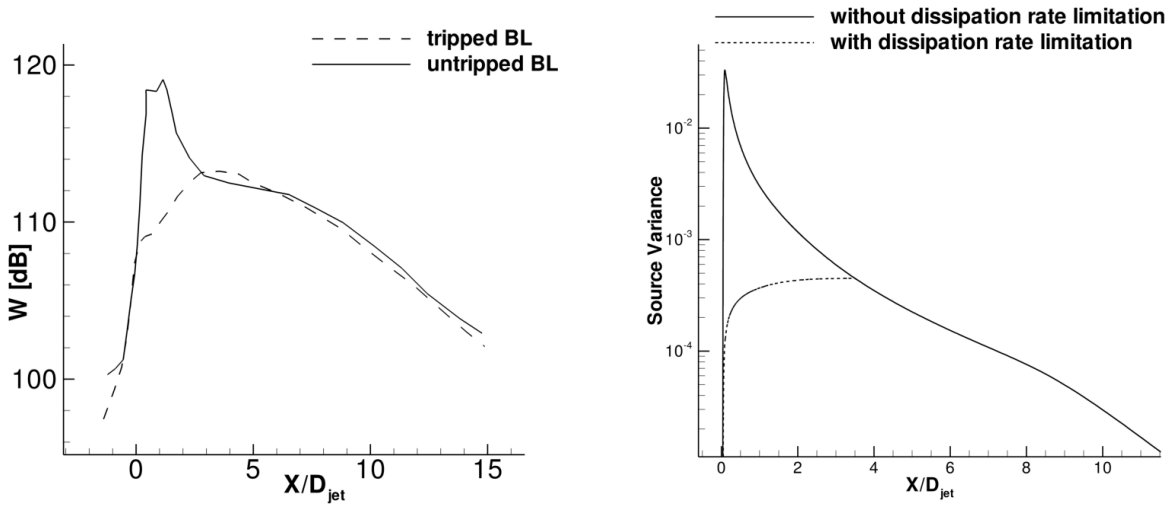

(a) (b)

Figure 5. Axial distribution of source strength with tripped and untripped boundary layer at nozzle exit: (a) Measurement with elliptic mirror technique by Grosche ($Ma = 0.7, D_{jet} = 20mm$), (b) Source variance distribution applied in RPM ($Ma = 0.75, D_{jet} = 0.5m$)

in Fig. 3(a). An observer position at $\theta = 90°$ and within the high frequency lobe at $\theta = 45°$ delivers then spectra, which are shown in Fig. 3(b). However, the radiation directions below $\theta = 60°$ are beyond the limits of the Tam & Auriault fine scale jet noise model. It is questionable, if the G-Spectrum is to expect at these angles.

By means of a turbulent dissipation rate limitation at the nozzle lip we could reach omni-directional noise radiation of G-Spectrum shape. The limitation has an effect up to $X/D = 3.5$ downstream of the nozzle Fig. 5, where the highest values in source variance occurred. Depending on the jet Mach number, the limitation value was chosen differently (e.g. for $Ma = 0.8 \rightarrow \omega \leq 25001/s$). This limitation influenced the variance as well as the time and length scale in the source model, where the strongest influence on high frequency excess noise was ascertained to come from the time scale. High frequency excess noise depending on the details of the nozzle lip boundary layer were also observed in the experiment by Grosche et al.[22] and in the LES computations of Bogey and Bailly.[20,21]

C. Effect of boundary layer thickness at nozzle lip

For better understanding of the physical reasons of high frequency excess noise further configurations, which influence the mean flow quantities at the origin of the shear layer were computed. The source variance peak at nozzle exit, which seems to have influence on excess noise radiation, could be drastically reduced, if a long pipe nozzle without contraction is used. The pipe nozzle with the length $\frac{L}{D_{jet}} = 16.5$, produces a thicker boundary layer at the nozzle exit than e.g. the double convergent nozzle, which is used in all other computations. In Fig. 6(a) the effect of the growing boundary layer thickness at the nozzle exit on the source variance $\hat{R}$ is shown. To be precise the quantity

$$\overline{k} = \frac{3\pi}{4l_s^2} \cdot \hat{R} \tag{23}$$

is shown here, with $\hat{R}$ as the source variance of the T&A model, i.e. $\hat{R} = \frac{4}{27} \frac{A^2 \cdot \rho_0^2 \cdot k^2}{\tau_s^2}$. Here is A the empirical constant of T&A-model and k the turbulent kinetic energy. The source variance can be expressed then as $\hat{R} = \frac{4}{3\pi} \cdot l_s^2 \cdot \overline{k}$, which represents $\hat{R} = \frac{\hat{q}_s^2}{c^2 \tau_s^2}$. As reference for reduction of $\overline{k}$ a pipe nozzle with the length $\frac{L}{D_{jet}} = 0.001$ is depicted in Fig. 6(a), too. The shear layer introduced with the pipe length 16.5 produces a spectra without excess noise as depicted in Fig. 7 at the observer position $\theta = 50°, 60°, 80°$. The spectrum in the Fig.7(a) is analysed for a Strouhal number range of 0.01 ... 10. The RPM-sources used in these

computations are depicted in Fig.6(b). All these spectra are analysed in the near-field as a preliminary evaluation. The extrapolation into far-field with the Ffowcs-Williams and Hawkings method is planed to be applied in the future.

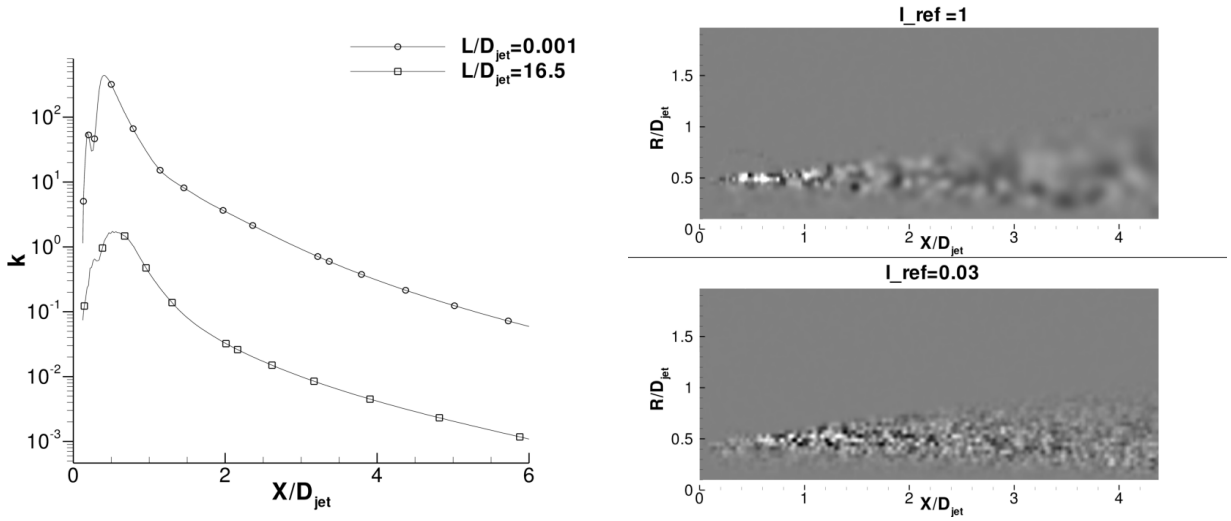

(a) (b)

Figure 6. (a) Axial distribution of $\overline{k}$ at $R/D_{jet} = 0.5$ for two different boundary layer thickness' at the nozzle trailing edge; (b) The sound sources of the pipe jet $\frac{L}{D_{jet}} = 16.5$ with scaling $l_{ref} = 1$ in the upper figure and $l_{ref} = 0.03$ in the lower figure

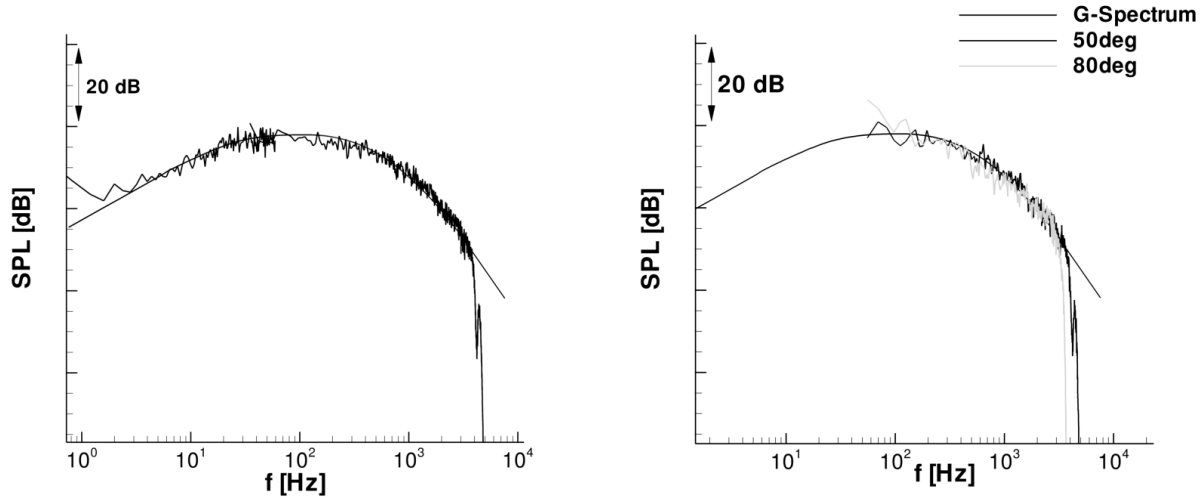

(a) (b)

Figure 7. Sound pressure level for jet noise of a pipe jet ($Ma = 0.75$) without mean flow gradients (a) in a range of $Str = 0.01 - 10$ at $\theta = 60°$ and (b) in a range of $Str = 0.2 - 10$ at $\theta = 50°$ and $\theta = 80°$

D. Mach scaling law

The computations with Mach number $Ma = 0.3, 0.5$ and 0.8, are used to analyze the Mach scaling exponent. This study is conducted for two-dimensional jets with Strouhal similarity correction and with dissipation rate limitation. The spectra in Fig. 4(b) are evaluated at $\theta = 45°$, at the position, where the excess noise is present with applied dissipation rate limitation. The Mach scaling exponent expected for a three dimensional

jet is $n = 8$. Since we are in 2-D, we would expect a $n = 7$, but PIANO delivers $n = 6.91$. The Mach scaling is also conducted in the 3-D modal computations, which is closer described in the Sec. V.

V. Extension to 3-D

The previous computations are conducted for two-dimensional jets. Recently, the method was extended to enable 3-D modal computations, allowing the simulation of 3-D jet noise based on the first three to five azimuthal modes at the computational cost of few 2-D CAA simulations. That only few first azimuthal modes of jet noise are sufficient for prediction was already observed in the measurements by Michalke[10] in the 80th. With the approach presented next we will be able to approve his observations numerically.

A. Azimuthal-modal linearized Euler equations decomposition

To perform azimuthal-modal computation of jet noise, we have to reformulate the governing equations (27) as linearized Euler equations in cylinder coordinates. This would enable thus decomposing the azimuthal varying variables into distinct azimuthal modes, eventually to perform selected modes as two simultaniously complex coupled computations. One equation set governs then the real part $\Re_{2-D}$ and the second the imaginary part $\Im_{2-D}$. At the end these equations would finally deliver a 3-D modal computation realized by sequentially/simultanously solved 2-D computation ($\Re_{2-D}$;$\Im_{2-D}$). The governing equations formulated in this way are utilized to propagate broadband jet noise, where all the frequencies of the resolved interval are present. Therefore, it is necessary also to cope with the imaginary part of the complex quantities. In the approach of Zhang et al.[18] e.g. the imaginary part is dispensed and only the real part is solved. This is possible, if a discrete frequency is considered, which is sufficient, if for instant one pretends to solve duct modes. There, the decoupling of real and imaginary part is realized at the cost of solving only one frequency. The decoupling is done by

$$\frac{\partial w'}{\partial \phi} = -\mathrm{i}mw', \quad \frac{\partial w'}{\partial t} = \mathrm{i}kw' \qquad \text{and} \qquad \frac{\partial p'}{\partial \phi} = -\mathrm{i}mp', \quad \frac{\partial p'}{\partial t} = \mathrm{i}kp' \tag{24}$$

which together results in the decoupled w' quantity in the mass equation with the cancelation of complex factor i

$$\frac{\partial w'}{\partial \phi} = -\frac{m}{k}\frac{\partial w'}{\partial t}. \tag{25}$$

and the decoupled sound pressure in the ϕ-momentum equation (time derivation deduced from the relationship of Eqn. (25))

$$\frac{\partial^2 p'}{\partial \phi \cdot \partial t} = mk \cdot p' \tag{26}$$

In the case of stochastic source modeling this decoupling is not realizable. Hence, two governing equation sets will be established, which are connected via the coupling terms. Starting with the Euler equations in conservative form

$$\begin{aligned} &\frac{\partial \rho}{\partial t} + \nabla \cdot (\rho \mathbf{u}) = 0 \\ &\frac{\partial (\rho \mathbf{u})}{\partial t} + \nabla \cdot (\rho \mathbf{u}\mathbf{u}) + \nabla p = \mathbf{0} \qquad (\rho, \mathbf{u}, p) \in \mathbb{R} \\ &\frac{\partial p}{\partial t} + \mathbf{u} \cdot \nabla p + \gamma p \nabla \cdot \mathbf{u} = Q_s, \end{aligned} \tag{27}$$

expressed in cylindrical coordinates the equations read

$$\begin{aligned} \frac{\partial \rho}{\partial t} + \frac{\partial (\rho u_x)}{\partial x} + \frac{1}{r}\frac{\partial (r\rho u_r)}{\partial r} + \frac{1}{r}\frac{\partial (\rho u_\phi)}{\partial \phi} &= 0 \\ \frac{\partial (\rho u_x)}{\partial t} + \frac{\partial (\rho u_x u_x)}{\partial x} + \frac{1}{r}\frac{\partial (r\rho u_r u_x)}{\partial r} + \frac{1}{r}\frac{\partial (\rho u_\phi u_x)}{\partial \phi} + \frac{\partial p}{\partial x} &= 0 \\ \frac{\partial (\rho u_r)}{\partial t} + \frac{\partial (\rho u_x u_r)}{\partial x} + \frac{1}{r}\frac{\partial (r\rho u_r u_r)}{\partial r} + \frac{1}{r}\frac{\partial (\rho u_\phi u_r)}{\partial \phi} + \frac{\partial p}{\partial r} &= 0 \end{aligned} \tag{28}$$

$$\frac{\partial(\rho u_\phi)}{\partial t}+\frac{\partial(\rho u_x u_\phi)}{\partial x}+\frac{1}{r}\frac{\partial(r\rho u_r u_\phi)}{\partial r}+\frac{1}{r}\frac{\partial(\rho u_\phi u_\phi)}{\partial \phi}+\frac{1}{r}\frac{\partial p}{\partial \phi} \qquad =0$$

$$\frac{\partial p}{\partial t}+u_x\frac{\partial p}{\partial x}+u_r\frac{\partial p}{\partial r}+\frac{u_\phi}{r}\frac{\partial p}{\partial \phi}+\gamma p\left(\frac{\partial u_x}{\partial x}+\frac{u_r}{r}+\frac{\partial u_r}{\partial r}+\frac{1}{r}\frac{\partial u_\phi}{\partial \phi}\right) \qquad =Q_s,$$

where Q_s is an acoustic source applied to the pressure equation. Here, all the flow quantities are real numbers. From this point on the LEE's can be derived from the Eqn. (28). The mean flow and the acoustic quantities $\rho^0, \mathbf{u}^0, p^0, \rho', \mathbf{u}', p'$, which appear in the LEE's can now be expanded as complex Fourier series (29). For the sake of simplicity the mean flow is assumed to be azimuthal independent i.e. only the perturbation quantities are modal decomposed, whereas the mean flow is only considered in its 0th mode (m=0, $u^0_\phi = 0$, $\{\rho^0, \mathbf{u}^0, p^0\} \in a$, $a = a_0(x,r,t)$). In further research the mean flow can be expressed in modal decompositions as well, which could be applied to more complex mean flow e.g. nozzle with serrations and/or swirl. Expressed as the Fourier series the perturbation quantities ($\{\rho', \mathbf{u}', p'\} \in b$ and $\hat{b} = b_\Re + \mathrm{i}b_\Im$) are:

$$b(x,r,\phi,t) = \sum_{m=-\infty}^{\infty} \hat{b}_m(x,r,t)\exp(\mathrm{i}m\phi) \qquad \hat{b}_m \in \mathbb{C} \tag{29}$$

The final form of the governing equations can be written then for the real computational domain as:

$$\begin{aligned}
&\frac{\partial \rho'_{\Re,m}}{\partial t}+u'_{x\Re,m}\frac{\partial \rho^0}{\partial x}+\rho^0\frac{\partial u'_{x\Re,m}}{\partial x}+u^0_x\frac{\partial \rho'_{\Re,m}}{\partial x}+\rho'_{\Re,m}\frac{\partial u^0_x}{\partial x}+\boxed{\frac{\rho^0 u'_{r\Re,m}}{r}} \\
&+\boxed{\frac{\rho'_{\Re,m}u^0_r}{r}}+\rho^0\frac{\partial u'_{r\Re,m}}{\partial r}+u'_{r\Re,m}\frac{\partial \rho^0}{\partial r}+\rho'_{\Re,m}\frac{\partial u^0_r}{\partial r}+u^0_r\frac{\partial \rho'_{\Re,m}}{\partial r}\boxed{\boxed{-\frac{m\rho^0}{r}u'_{\phi\Im,m}}} &=0 \\
&\frac{\partial u'_{x\Re,m}}{\partial t}+u'_{x\Re,m}\frac{\partial u^0_x}{\partial x}+u^0_x\frac{\partial u'_{x\Re,m}}{\partial x}+u'_{r\Re,m}\frac{\partial u^0_x}{\partial r}+u^0_r\frac{\partial u'_{x\Re,m}}{\partial r}-\frac{\rho'_{\Re,m}}{(\rho^0)^2}\frac{\partial p^0}{\partial x}+\frac{1}{\rho^0}\frac{\partial p'_{\Re,m}}{\partial x} &=0 \\
&\frac{\partial u'_{r\Re,m}}{\partial t}+u'_{x\Re,m}\frac{\partial u^0_r}{\partial x}+u^0_x\frac{\partial u'_{r\Re,m}}{\partial x}+u'_{r\Re,m}\frac{\partial u^0_r}{\partial r}+u^0_r\frac{\partial u'_{r\Re,m}}{\partial r}-\frac{\rho'_{\Re,m}}{(\rho^0)^2}\frac{\partial p^0}{\partial r}+\frac{1}{\rho^0}\frac{\partial p'_{\Re,m}}{\partial r} &=0 \\
&\frac{\partial u'_{\phi\Re,m}}{\partial t}+u^0_x\frac{\partial u'_{\phi\Re,m}}{\partial x}+u^0_r\frac{\partial u'_{\phi\Re,m}}{\partial r}+\boxed{\frac{u^0_r u'_{\phi\Re,m}}{r}}\boxed{\boxed{-\frac{m}{r\rho^0}p'_{\Im,m}}} &=0 \\
&\frac{\partial p'_{\Re,m}}{\partial t}+u'_{x\Re,m}\frac{\partial p^0}{\partial x}+u^0_x\frac{\partial p'_{\Re,m}}{\partial x}+u'_{r\Re,m}\frac{\partial p^0}{\partial r}+u^0_r\frac{\partial p'_{\Re,m}}{\partial r} \\
&+\gamma p^0\left(\frac{\partial u'_{x\Re,m}}{\partial x}+\boxed{\frac{u'_{r\Re,m}}{r}}+\frac{\partial u'_{r\Re,m}}{\partial r}\boxed{\boxed{-\frac{m}{r}u'_{\phi\Im,m}}}\right)+\gamma p'_{\Re,m}\left(\frac{\partial u^0_x}{\partial x}+\boxed{\frac{u^0_r}{r}}+\frac{\partial u^0_r}{\partial r}\right) &=\hat{Q}_{s\Re}
\end{aligned} \tag{30}$$

The terms within the single box represent the additional cylindrical terms, which are not present in the cartesian formulation of LEE's. The terms in the double box are the coupling terms, which connect the imaginary governing equations with the real. The coupling nature of this terms comes from the relationship shown examplary for density equation in the Eqn. (31). For the imaginary domain the governing equations have in principle the same form, with the difference that the coupling terms there are positive.

$$\begin{aligned}
&\frac{\rho^0}{r}\cdot \mathrm{i}m\cdot\left[\Re(u'_{\phi,m})+\mathrm{i}\Im(u'_{\phi,m})\right] \\
=\quad &\frac{m\rho^0}{r}\cdot\left[-\Im(u'_{\phi,m})+\mathrm{i}\Re(u'_{\phi,m})\right]
\end{aligned} \tag{31}$$

In further development to increase the efficiency of the implemented LEE's it is also thinkable to apply the equations in the way, that several 2-D planes are located in the third dimension as a single 3-D grid. Since there are no derivatives or any other exchanges of values in third dimension in the governing equations, the planes would be solved completly independent. That would allow to simulate chosen number of modes within a single computation. If the extension of the equations with the azimuthal decomposition mean flow arises, cross dependencies between acoustic and mean flow modes would appear. The advantage of such an approach is that all the values of the regarded modes are accessible during the computation and all cross-denpendend modes can be readily computed.

B. Boundary Conditions

With the aim to verify the implemented LEE's several test cases with an annular duct as well as circular duct mode radiation into free field were conducted. Thereby we closely followed the configurations published by Li et al.[15] and Zhang et al.[18] This cases were in the sense appropriate for the verification, since there are available well-defined analytic solutions and also published results of azimuthal decomposed numerically computed duct mode propagations. To initiate the azimuthal-radial acoustic duct modes in an annular/circular duct the forcing sponge layer boundary condition (BC) is used. Not all BC's provided by PIANO for the genuine LEE's can be applied in conjunction with azimuthal decomposed equations. The only BC's which hold at the moment are the solid wall BC, the sponge layer (SL) BC and the slip wall BC. For the test cases with annular duct all boundaries are set to slip wall BC. Additionally, at the incoming boundary a forcing SL was defined and at the outgoing boundary a damping SL was placed to take the acoustic energy out of the computational domain. The additional term on the RHS, which is activated with the SL is

$$-\sigma(\xi)(u' - u_{ref}) \quad \text{with the fading function } \sigma(\xi) = \frac{1}{2}\left(1 - \cos\left(\frac{\xi \cdot \pi}{d_{SL}}\right)\right), \tag{32}$$

where ξ is the local position normal to the boundary edge within the SL and d_{SL} is the SL width. For the damping SL u_{ref} is set to 0, which forces all the perturbation quantities to damp out, providing the wave length is smaller than the SL width. For the forcing SL an arbitrarily chosen function $u_{ref}(\xi, t)$ can be imposed onto the computational domain to enforce incoming perturbations, which is utilized here to let the duct modes enter the domain.

The modes are initiated in both domains, in the real and imaginary domain at the inflow BC with a phase shift of $\phi = \arctan\left(\frac{\Im}{\Re}\right) = 90°$. For the determination of a general forcing function e.g. for pressure in positive propagating direction of the modes, a separation of variables ansatz is applied,

$$\begin{aligned}\hat{p}(x, r, \theta, t) &= A^+_{mn} \cdot \mathrm{e}^{-\mathrm{i}k^+_{mn} \cdot x} \cdot \mathrm{e}^{-\mathrm{i}m \cdot \theta} \cdot \mathrm{e}^{\mathrm{i}k \cdot t} \cdot f_{mn}(r) \\ &= A^+_{mn} \cdot \left(\underbrace{\cos(k \cdot t - k^+_{mn} \cdot x - m \cdot \theta)}_{\Re} + \underbrace{\mathrm{i} \cdot \sin(k \cdot t - k^+_{mn} \cdot x - m \cdot \theta)}_{\Im} \right) \cdot f_{mn}(r)\end{aligned} \tag{33}$$

where A^+_{mn} is the aplitude of described duct mode, $f_{mn}(r)$ is a function describing the radial shape of the duct mode and the trigonometrical functions describe the space-time propagation of the mode. The physical solution is provided by the real part of this ansatz. A Fourier series decomposition applied to this part yields

$$\hat{p}_m(x, r, t) = \frac{1}{2\pi} \int_{-\pi}^{\pi} \Re(\hat{p}(x, r, \theta, t)) \cdot \mathrm{e}^{-\mathrm{i}m_F\theta} \mathrm{d}\theta \tag{34}$$

Strictly speaking the mode m_F represents not the same variable as the m of the duct mode, but which should both be in coincidence. That means, only if $m = m_F$ the integral is non-zero, all other combinations of m and m_F do not contribute to the final solution. For the case $m = m_F$ the forcing function for the pressure is given then in the form

$$\hat{p}_m(x, r, t) = \frac{1}{2} \cdot A^+_{mn} \cdot f_{mn}(r) \left(\cos(k \cdot t - k^+_{mn} \cdot x) - \mathrm{i} \sin(k \cdot t - k^+_{mn} \cdot x)\right), \tag{35}$$

which describes the real and imaginary part of the modes. The other acoustic perturbation quantities are derived in the same way, which are given in the final form as

Real:

$$\begin{aligned}\rho'(x, r, t) &= p'(x, r, t) \\ u'(x, r, t) &= \frac{1}{\rho_0} \frac{k^+_{mn}}{(k - u_0 k^+_{mn})} A^+_{mn} \cdot \cos(kt - k^+_{mn} x) \cdot f_{mn}(r) \\ v'(x, r, t) &= -\frac{1}{\rho_0} \cdot \frac{1}{(k - u_0 k^+_{mn})} \cdot A^+_{mn} \cdot \sin(kt - k^+_{mn} x) \cdot \frac{\partial f_{mn}(r)}{\partial r} \\ w'(x, r, t) &= \frac{1}{\rho_0 r} \frac{m}{(k - u_0 k^+_{mn})} A^+_{mn} \cdot \cos(kt - k^+_{mn} x) \cdot f_{mn}(r)\end{aligned}$$

(36)

Imaginary:
$$\begin{aligned}
\rho'(x,r,t) &= p'(x,r,t) \\
u'(x,r,t) &= \frac{1}{\rho_0}\frac{k^+_{mn}}{(k-u_0k^+_{mn})}A^+_{mn}\cdot\sin(kt-k^+_{mn}x)\cdot f_{mn}(r) \\
v'(x,r,t) &= \frac{1}{\rho_0}\cdot\frac{1}{(k-u_0k^+_{mn})}\cdot A^+_{mn}\cdot\cos(kt-k^+_{mn}x)\cdot\frac{\partial f_{mn}(r)}{\partial r} \\
w'(x,r,t) &= \frac{1}{\rho_0 r}\frac{m}{(k-u_0k^+_{mn})}A^+_{mn}\cdot\sin(kt-k^+_{mn}x)\cdot f_{mn}(r)
\end{aligned} \tag{37}$$

In the annular duct the propagating modes are to determine by the computation of inner and outer roots of the eigenform function f_{mn},

$$f_{mn}(r) = J_m(\alpha_{mn}\cdot r) + Q_{mn}Y_m(\alpha_{mn}\cdot r), \tag{38}$$

where the eigenform function is described by Bessel J_m and Neumann Y_m functions. To compute the constant Q_{mn} for the chosen radii following conditions have to be satisfied:

$$\begin{aligned}
\frac{\partial J_m(\sigma_{mn,i})}{\partial r} + Q_{mn}\frac{\partial Y_m(\sigma_{mn,i})}{\partial r} &= 0 \\
\frac{\partial J_m(\sigma_{mn,o})}{\partial r} + Q_{mn}\frac{\partial Y_m(\sigma_{mn,o})}{\partial r} &= 0
\end{aligned} \tag{39}$$

Since the Q_{mn} has to be satisfied for inner and outer radius, the above conditions have to be combined to

$$\frac{\partial J_m(\sigma_{mn,o})}{\partial r}\cdot\frac{\partial Y_m(\sigma_{mn,i})}{\partial r} - \frac{\partial J_m(\sigma_{mn,i})}{\partial r}\cdot\frac{\partial Y_m(\sigma_{mn,o})}{\partial r} = 0 \tag{40}$$

to determine the corresponding σ_{mn}. The relation between α_{mn} and σ_{mn} is

$$\sigma^2_{mn,o} = \alpha^2_{mn}\cdot r^2_o \qquad \text{and} \qquad \sigma^2_{mn,i} = \alpha^2_{mn}\cdot r^2_i \tag{41}$$

where the indices i indicates the inner and the o the outer radius. The α_{mn} represents the radial wave number. If we regard a circular duct, the form function simplifies to the form

$$f_{mn}(r) = J_m(\alpha_{mn}\cdot r) \tag{42}$$

with the hard wall boundary condition

$$\frac{\partial J_m(\sigma_{mn,o})}{\partial r} = 0. \tag{43}$$

C. Verification of implemented governing equations via duct modes

In the test case with the duct modes radiation into free field, which is shown in Fig. (8), good agreement was achieved in comparison to the results published by Zhang.[18] In this configuration the waves are running against the uniform mean flow with $Ma = -0.5$. The mode is of azimuthal order $m = 13$ and radial order $n = 1$. At the starting end of the duct the forcing sponge layer was applied, which goes from $x = -1.5 \ldots -0.8$. At the outer boundaries, a damping sponge layer is applied, which should avoid reflections and amplification of emitted sound. The test cases with the annular duct correspond to a configuration of a engine intake i.e. the acoustic modes run against the mean flow (refer to Li et al.[15]). Different azimuthal and radial modes are simulated to prove the ability of implemented equations to compute azimuthal decomposed problems. In the Fig. 10(a)-(d) and in Fig. 11(e)-(g) the duct modes $(m,n) = (0,1);(1,1);(1,2);(1,3);(5,1);(5,2);(10,1)$ are shown as contour plot of the sound pressure, the axial distribution and the radial shape at the position with the maximum amplitude. Quite a good agreement is observed between analytical and simulated results.

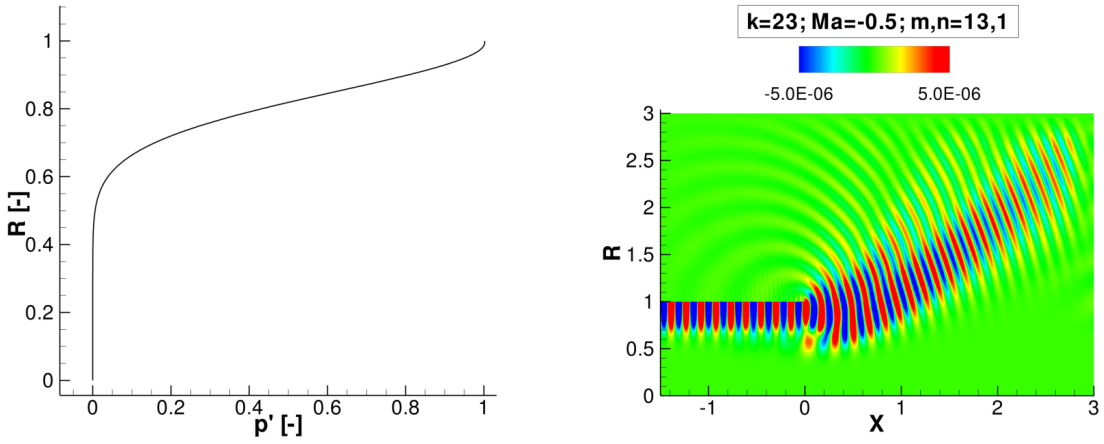

(a) (b)

Figure 8. Radial shape (a) and the sound pressure distribution (b) of the the enforced duct mode (m=13, n=1, Ma=-0.5, k=23.0)

D. Radial RPM-source filtering for 3-D modal jet noise

The modeling of RPM-sources in 3-D modal space needs a reformulation, which would transform the physical 3-D sources into the 3-D modal sources. Accordingly to the LEE's, the Fourier series decomposition is used as well on the source correlations to provide the simulated mode with the corresponding sources. Hence, the physical source is a summation of all azimuthal source modes:

$$\theta(x,r,\phi,t) = \sum_{m=-\infty}^{m=\infty} \hat{\theta}_m(x,r,t)\exp(im\phi) \qquad \hat{\theta}_m \in \mathbb{C} \tag{44}$$

where $\theta \equiv \frac{Dq_s}{Dt}$. If it is applied to RPM the Eqn. (5) changes its filter kernel to $\hat{G}_m$, which means that for each mode a different universally valid radial filter kernel is used. For more details concerning the decomposition of RPM-sources refer to Ewert et al.[8]

E. Results

For 3-D modal computations the RANS-data for a jet of $Ma = 0.75$ was chosen. The azimuthal modes of order $m = 0 \ldots 5$ are computed and the SPL spectra at different observer positons in the near field are evaluated. In these computations the mean flow gradients are activated. An arc of 31 virtual microphones is positioned in the computational domain with the circle center at $R/D_{jet} = -100$, $X/D_{jet} = 10$ and circle radius $R = 110$ (i.e. the microphones are located almost parallel to the jet axis). The contour plots of the sound pressure of these computations are depicted in Fig. 12,13 and 14 for real and imaginary parts. The real and imaginary domains are stochasticaly completly independent, but generate both qualitatively the same sound pressure field. The spectra of each azimuthal mode at four different polar angles $\theta = 70°, 60°, 30°$ and $20°$ (measured from the jet axis) are shown separatelly and as the sum of all 6 computed modes, which is depicted in Fig. 9(a)-(d). As it was expected, the contribution of the higher modes is less important than that of the zeroth azimuthal mode. The higher modes gain its importance only at high Strouhal numbers and can be neglected at Strouhal numbers below $Str = 1.0$. To compare these spectra with the shape of the G- and F-Spectra, these are also depicted in the figures, where the comparison shows quite good agreement as well for G-Spectum as for F-Spectrum. At the moment, the spectra cover a small part of the similarity spectra, since a short sampling time was computed due to the lack of time. A broader band of Strouhal number is expected to predict G-Spectrum in coming computations, as it was already shown in 2-D computations.

The Mach scaling law was analysed with the 3-D modal LEE's for 3 different Mach numbers $Ma = 0.3, 0.5, 0.75$, which are shown in Fig. 15 as contour plots of sound pressure. The spectra of these computations

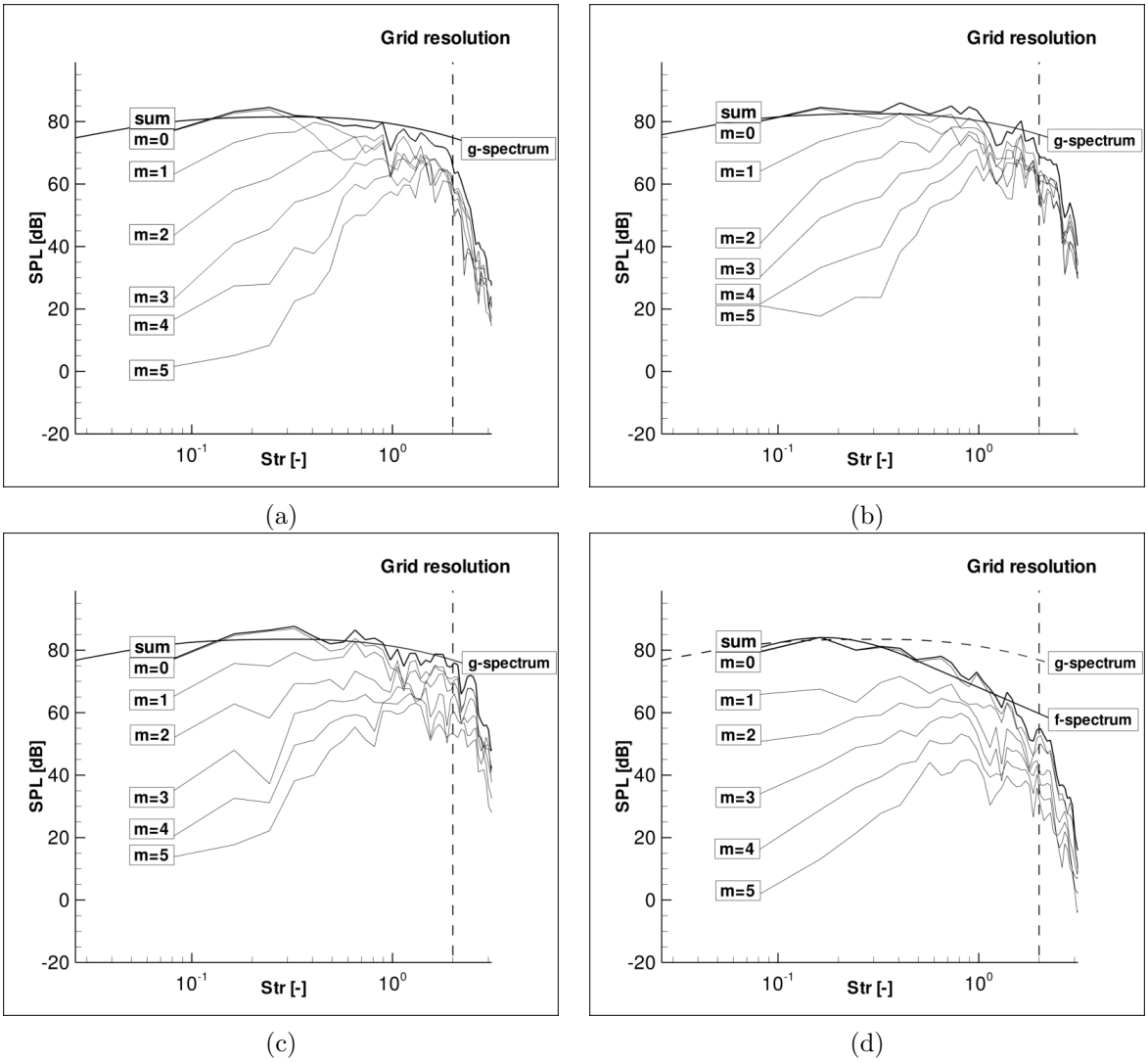

Figure 9. Sound pressure level spectra at observer angle (a) $\theta = 70°$, (b) $\theta = 60°$, (c) $\theta = 30°$ and (d) $\theta = 20°$ for azimuthal mode orders $m = 0, 1, 2, 3, 4, 5$ and the sum spectrum in comparison to G-Spectrum for a cold SSJ $Ma = 0.75$

at the angles $\theta = 80°, 30°$ are depicted in Fig. 16. These spectra perform a Mach scaling law of $n = 7.2$ at $\theta = 80°$ and $n = 8.1$ at $\theta = 30°$.

VI. Computations with mean flow gradients

By activating mean flow gradients, large scale noise is activated, which leads to F-Spectra at shallow angles. In 2-D computations, we could observe continuous transition from a G-Spectrum to a F-Spectrum, going from $\theta = 90°$ to $\theta = 30°$, refer to Fig. 4(a). The radial position of the virtual microphones, labeled with sequentially increasing numbers for decreasing angles, is roughly at $R/D_{jet} = 10$, slightly decreasing downstream. The terms named in Eqn. (45), which are responsible for triggering of large scale noise, cause an interaction of the RPM-sources with the meanflow in the vicinity of the nozzle.

Density equation: $\hat{u}'_{xm}\dfrac{\partial \rho^0}{\partial x}$; $u'_{rm}\dfrac{\partial \rho^0}{\partial r}$; $\hat{\rho}'_m\dfrac{\partial u_x^0}{\partial x}$; $\hat{\rho}'_m\dfrac{\partial u_r^0}{\partial r}$; $\dfrac{\hat{\rho}'_m u_r^0}{r}$;

x-momentum equation: $\hat{u}'_{xm}\dfrac{\partial u_x^0}{\partial x}$; $\hat{u}'_{rm}\dfrac{\partial u_x^0}{\partial r}$; $-\dfrac{\hat{\rho}'_m}{(\rho^0)^2}\dfrac{\partial p^0}{\partial x}$;

$$\begin{array}{lllllll} \textbf{r-momentum equation:} & \hat{u}'_{xm}\dfrac{\partial u_r^0}{\partial x}; & \hat{u}'_{rm}\dfrac{\partial u_r^0}{\partial r}; & -\dfrac{\hat{\rho}'_m}{(\rho^0)^2}\dfrac{\partial p^0}{\partial r}; & & & \\ \textbf{Pressure equation:} & \hat{u}'_{xm}\dfrac{\partial p^0}{\partial x}; & u'_{rm}\dfrac{\partial p^0}{\partial r}; & \gamma\hat{p}'_m\dfrac{\partial u_x^0}{\partial x}; & \gamma\hat{p}'_m\dfrac{\partial u_r^0}{\partial r}; & \gamma\dfrac{\hat{p}'_m u_r^0}{r}; & \end{array} \tag{45}$$

which are neglected in the computations, where only the fine scale noise is considered. That means, that in the computations with mean flow gradients the above terms should be included in the governing equations of fine scale noise, which were

$$\begin{aligned} \frac{\partial \rho'_m}{\partial t} + u_x^0\frac{\partial \rho'_m}{\partial x} + u_r^0\frac{\partial \rho'_m}{\partial r} + \rho^0\left(\frac{\partial u'_{x,m}}{\partial x} + \frac{\partial u'_{r,m}}{\partial r} + \frac{u'_{r,m}}{r}\boxed{-\tfrac{m}{r}u'_{\phi,m}}\right) &= 0 \\ \frac{\partial u'_{x,m}}{\partial t} + u_x^0\frac{\partial u'_{x,m}}{\partial x} + u_r^0\frac{\partial u'_{x,m}}{\partial r} + \frac{1}{\rho^0}\frac{\partial p'_m}{\partial x} &= 0 \\ \frac{\partial u'_{r,m}}{\partial t} + u_x^0\frac{\partial u'_{r,m}}{\partial x} + u_r^0\frac{\partial u'_{r,m}}{\partial r} + \frac{1}{\rho^0}\frac{\partial p'_m}{\partial r} &= 0 \\ \frac{\partial u'_{\phi,m}}{\partial t} + u_x^0\frac{\partial u'_{\phi,m}}{\partial x} + u_r^0\frac{\partial u'_{\phi,m}}{\partial r} + \frac{u_r^0 u'_{\phi,m}}{r}\boxed{-\tfrac{m}{r\rho^0}p'_m} &= 0 \\ \frac{\partial p'_m}{\partial t} + u_x^0\frac{\partial p'_m}{\partial x} + u_r^0\frac{\partial p'_m}{\partial r} + \gamma p^0\left(\frac{\partial u'_{x,m}}{\partial x} + \frac{\partial u'_{r,m}}{\partial r} + \frac{u'_{r,m}}{r}\boxed{-\tfrac{m}{r}u'_{\phi,m}}\right) &= \hat{Q}_s \end{aligned} \tag{46}$$

VII. Conclusions

A 3-D modal approach embedded in a finite difference time-domain CAA code has been verified and applied to jet noise. Two sets of governing equations were established to simulate the real and imaginary part of azimuthal decomposed acoustical quantities. To simulate the acoustical sources, the RPM method based on the source model formulated by Tam & Auriault has been used. The RPM method has been azimuthal decomposed in the corresponding manner as the governing equations to provide the CAA with correct sources. Different nozzle configurations with variations in jet exit velocity and jet diameter have been computed as 2-D and as 3-D modal jets. The spectra at different observer positions have been evaluted in a rang of $\theta = 90^\circ$ ... 20°. The results show that with growing azimuthal mode order the acoustical contribution decreases rapidly. Therefore, it is not necessary to consider a large number of modes. The analysis of the Mach scaling law shows a slight variation in the scaling exponent dependent on observer position. At present, only the near field predictions have been evaluated and compared with the similarity spectra of jet noise. In the future, it is planed to extend the code with the Ffowcs-Williams and Hawking method to extrapolate the near-field predictions to far-field.

Figures

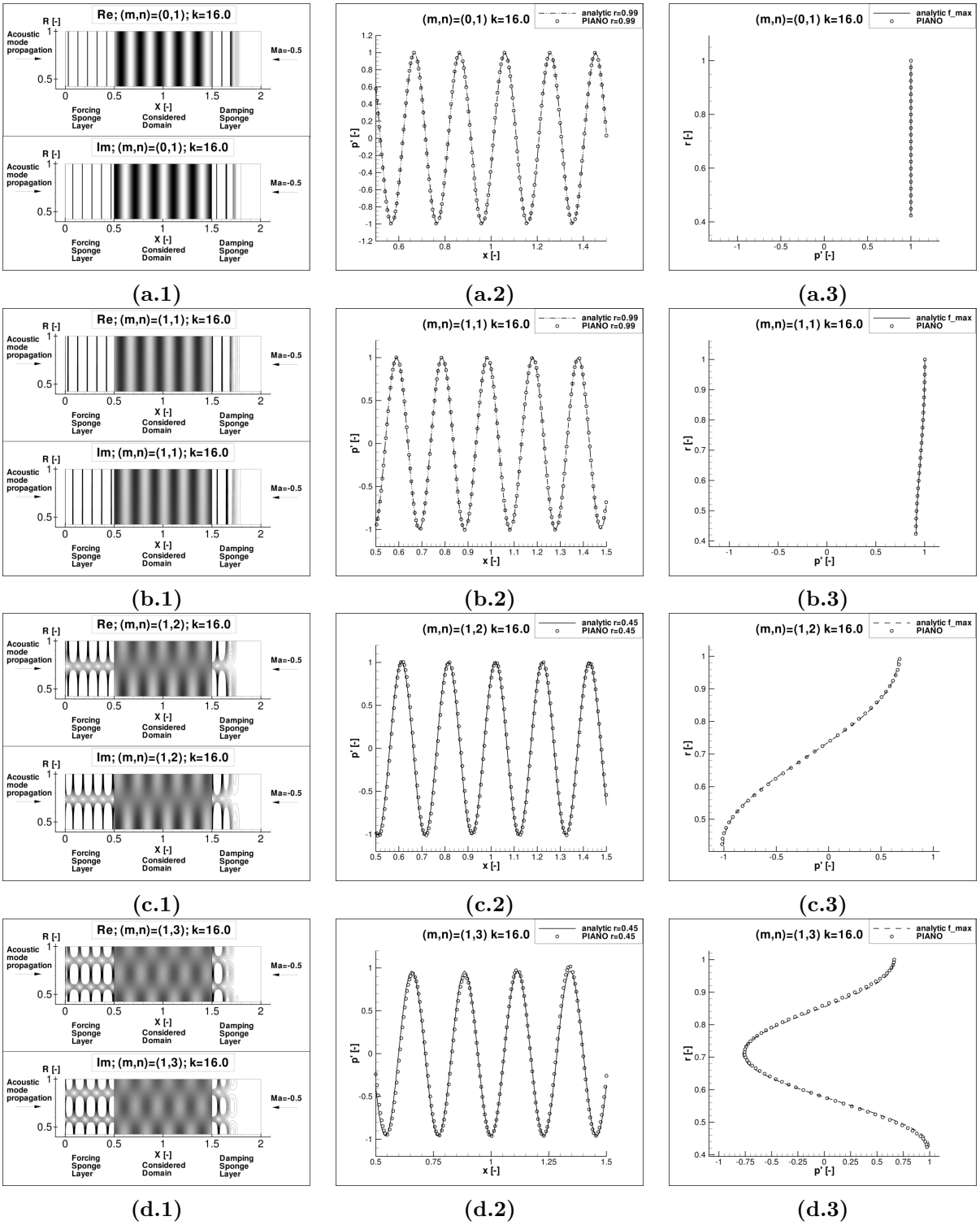

Figure 10. Annular duct modes computed by azimuthal decomposed LEE's in comparison to analytic solution ($k = 16.0,\ Ma = -0.5$)

vspace4cm

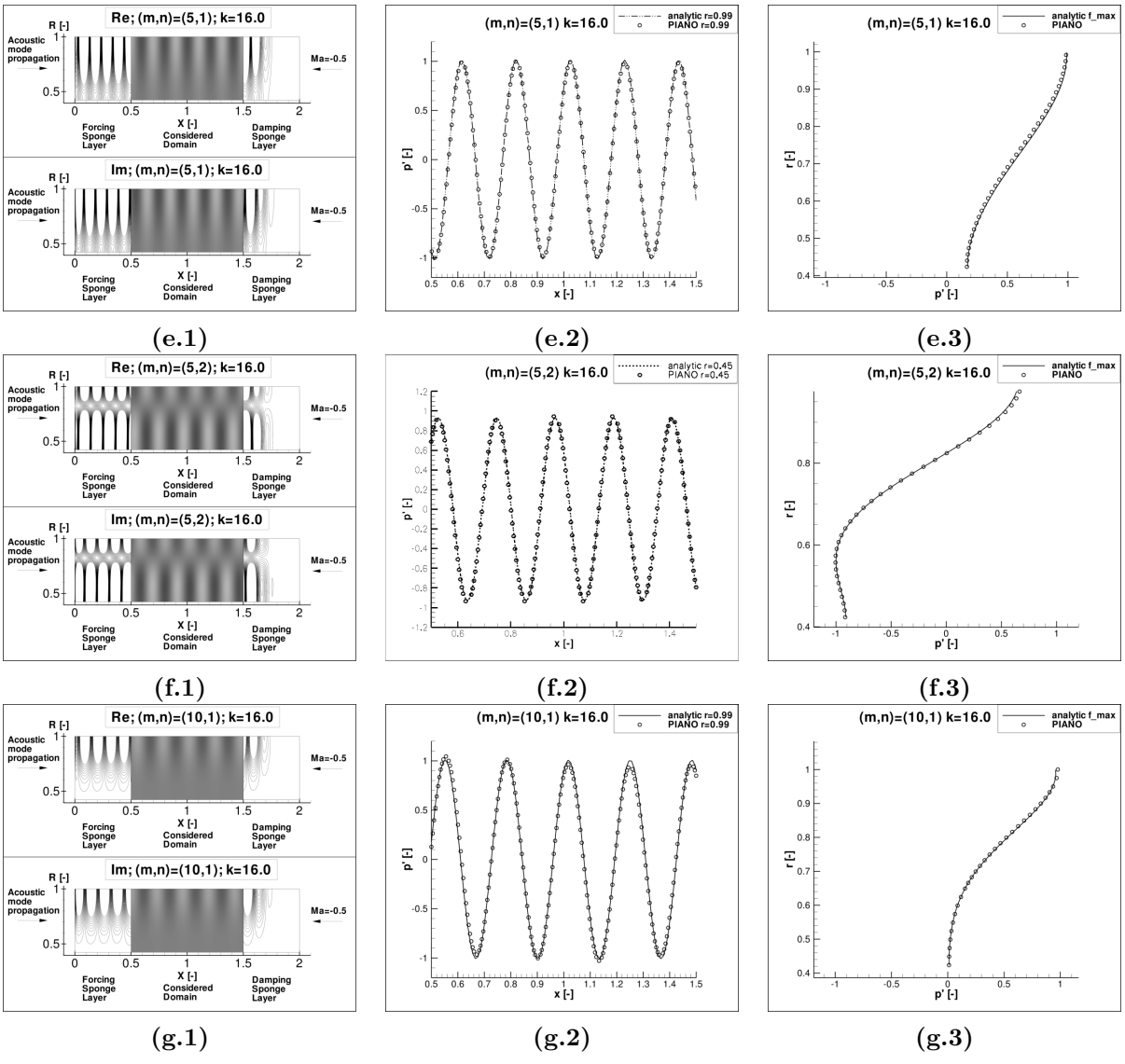

Figure 11. Annular duct modes computed by azimuthal decomposed LEE's in comparison to analytic solution ($k = 16.0,\ Ma = -0.5$)

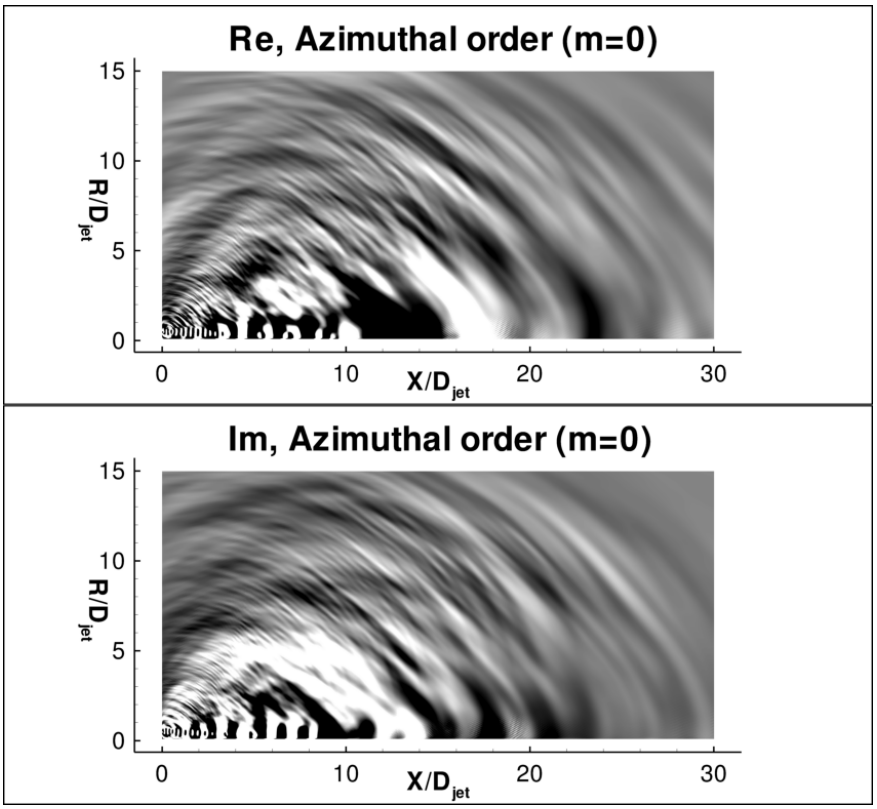

(a)

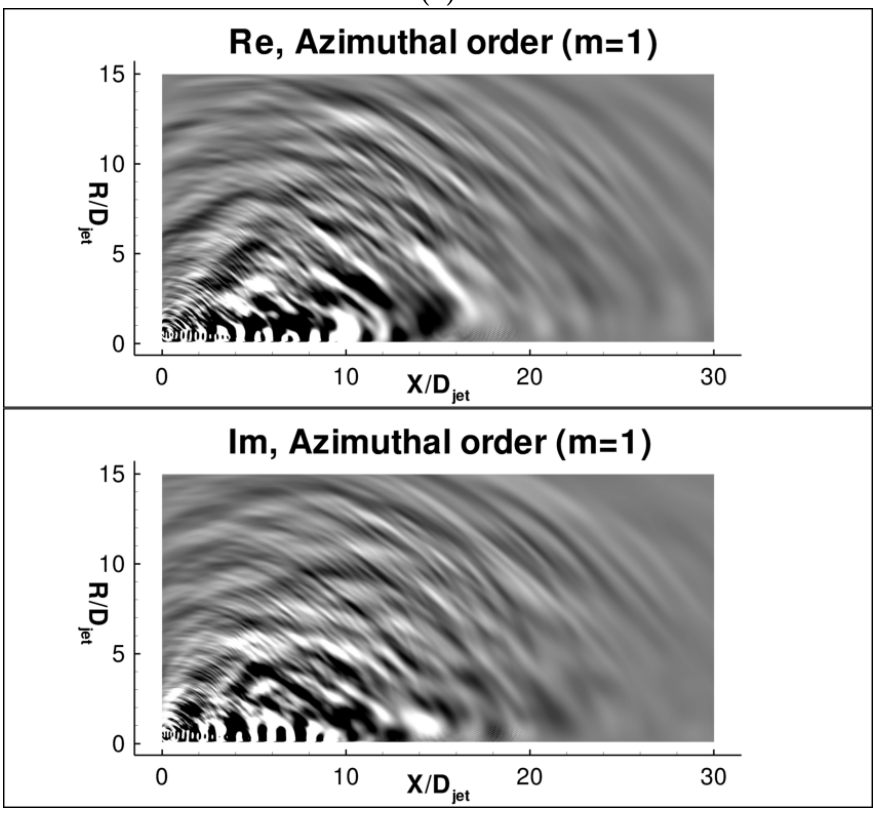

(b)

Figure 12. Sound pressure distribution for jet noise with mean flow gradients for mode order (a) $m = 0$ and (b) $m = 1$ (SSJ cold jet, $Ma = 0.75$)

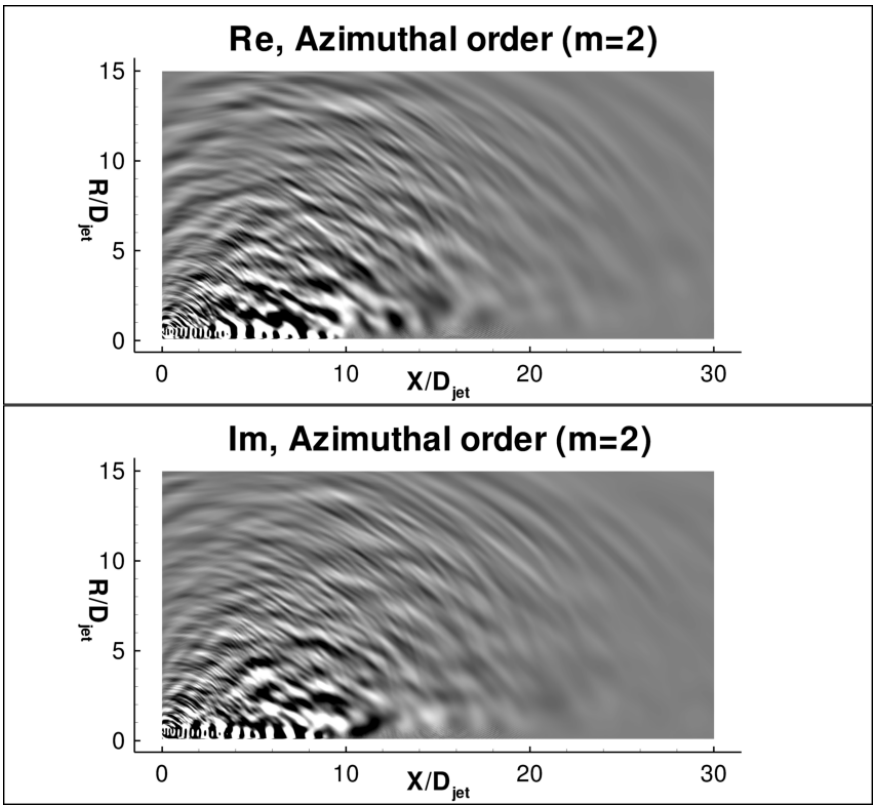

(a)

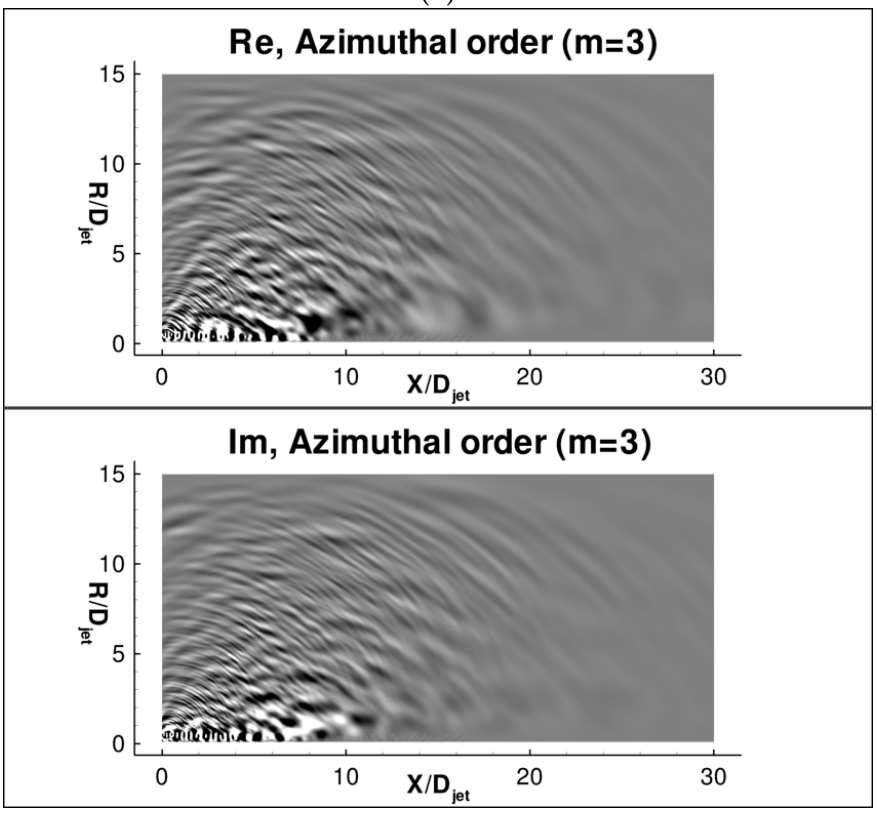

(b)

Figure 13. Sound pressure distribution for jet noise with mean flow gradients for mode order (a) $m = 2$ and (b) $m = 3$ (SSJ cold jet, $Ma = 0.75$)

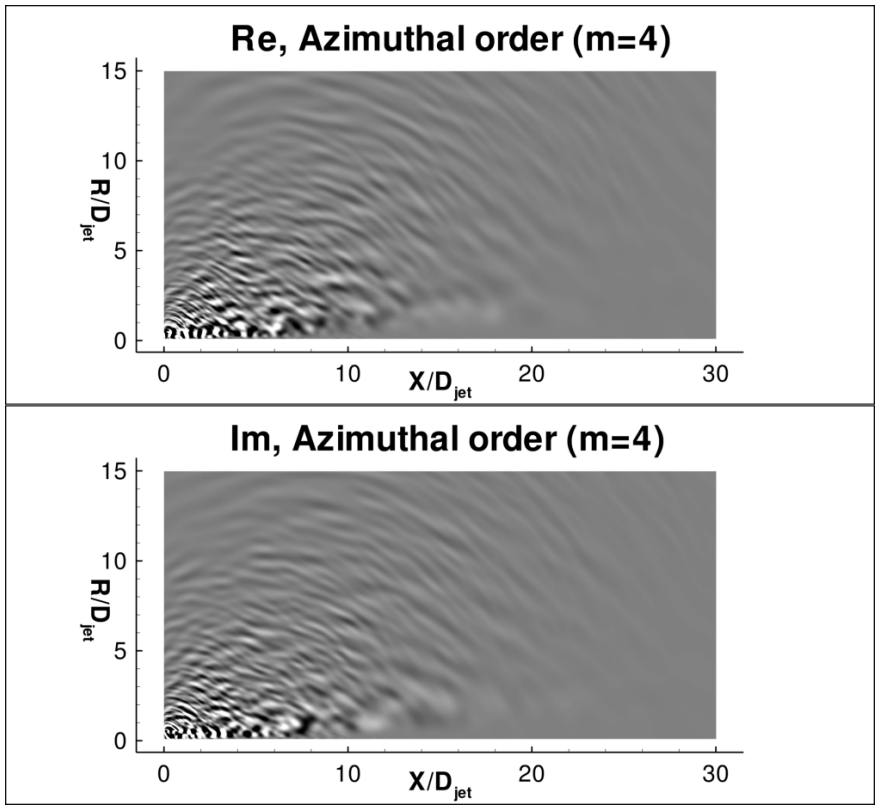

(a)

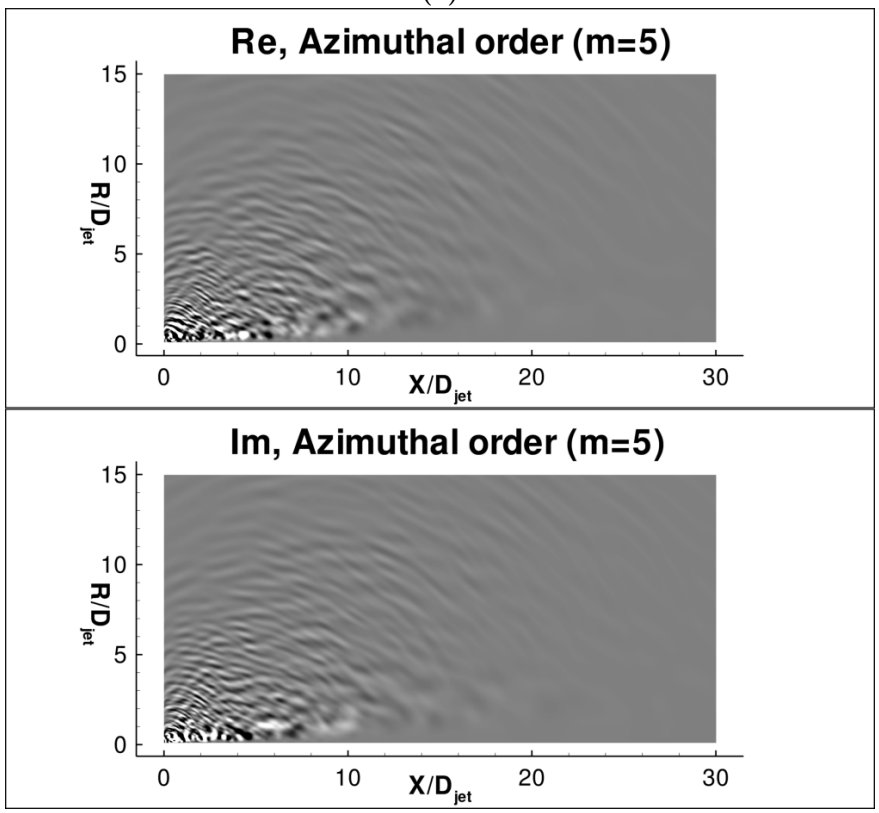

(b)

Figure 14. Pressure distribution for jet noise with mean flow gradients for mode order (a) $m = 4$ and (b) $m = 5$ (SSJ cold jet, $Ma = 0.75$)

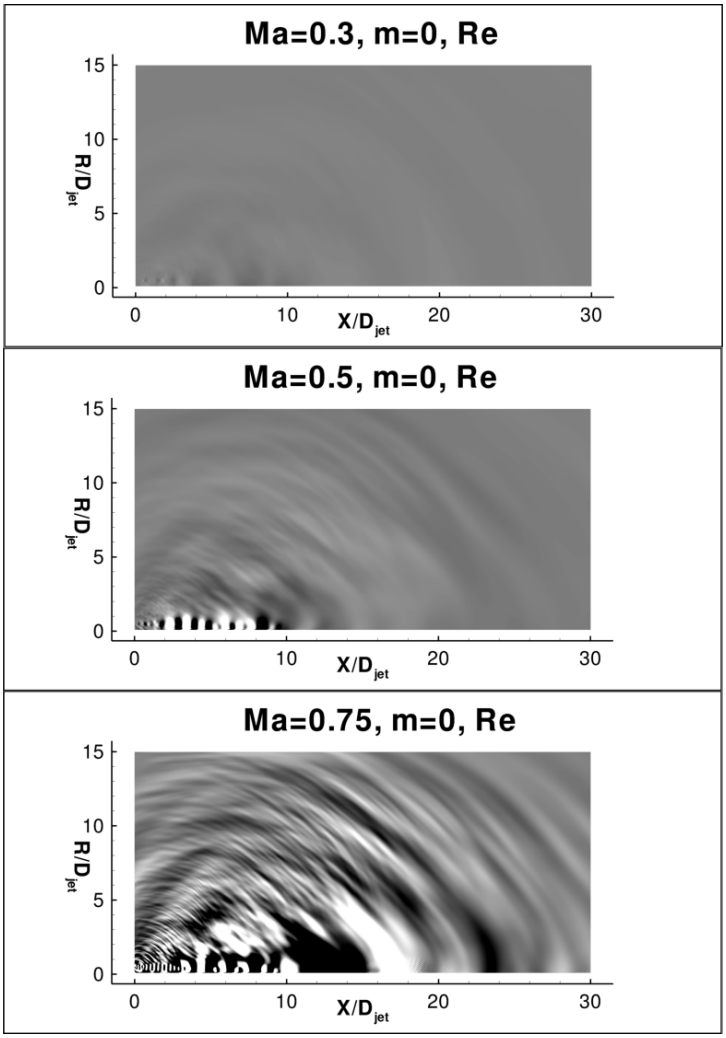

Figure 15. Sound pressure distribution for jet noise ($Ma = 0.3, 0.5, 0.75$) with mean flow gradients for mode order $m = 0$ with frequency resolution up to $Str = 2$

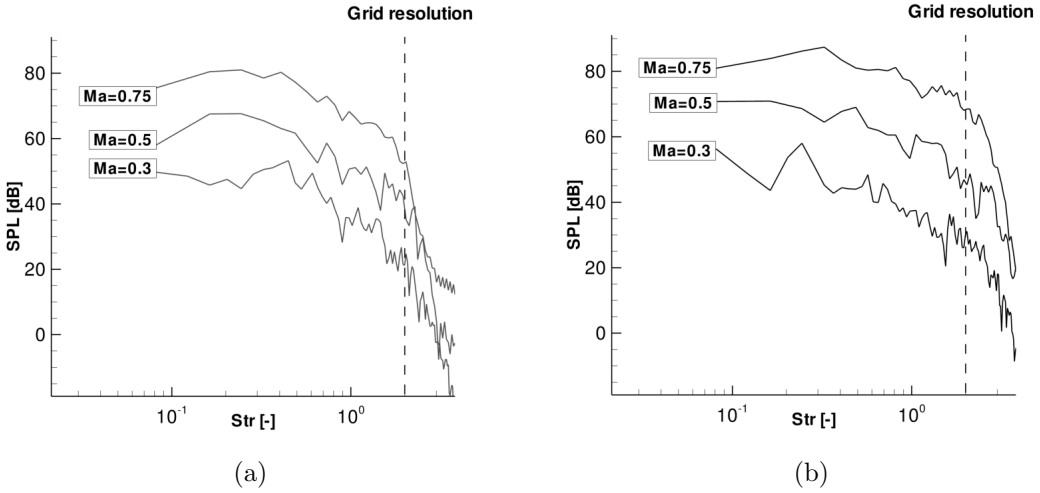

Figure 16. Sound pressure level for jets with $Ma = 0.3, 0.5, 0.75$ at the angle (a) $\theta = 80^\circ$ and (b) $\theta = 30^\circ$

Acknowledgments

This work was done in a framework of the OPTITHECK project in collaboration with Rolls-Royce Deutschland, Functional Systems Engineering, Aerodynamics & Acoustics. Special thanks to Dr. M.Trumper and Dr. M.Rose for their valuable contribution to this work and to Prof. J.W.Delfs for his guidance during the project. The computational time is provided by Center for Computer Applications in AeroSpace Science and Engineering ($C^2A^2S^2E$).

References

[1]Tam, C.K.W. and Webb, J.C., "Dispersion-relation-preserving finite difference schemes for computational acoustics", J. of Computational Physics Vol. 107, Issue 2, Aug. 1993.

[2]Tam, C.K.W. and Auriault, L., "Jet mixing noise from fine-scale turbulence", AIAA Vol. 37, No. 2, February 1999.

[3]Tam, C.K.W.,Pastouchenko, N. and Auriault, L., "Effects of Forward Flight on Jet Mixing Noise from Fine-Scale Turbulence", AIAA Vol. 39, No. 7, July 2001.

[4]Tam, C.K.W. and Auriault, L., "Mean flow refraction effects on sound radiated from localized sources in a jet", Journal of Fluid Mechanics Vol. 370, pp. 149-174, March 1998.

[5]Ewert, R., "RPM - the fast Random Particle-Mesh method to realize unsteady turbulent sound sources and velocity fields for CAA applications", AIAA 2007-3506.

[6]Ewert, R., Kornow, O., J, Yin, Delfs, J.W., Röber, T. and Rose, M., "A CAA Based Approach to Tone Haystacking", 15th AIAA/CEAS Aeroacoustics Conference 2009-3217, May 2009, Miami, Florida.

[7]Ewert, R., Dierke, J., Muehlbauer, B, Neifeld, A., Appel, C., Siefert, M., Kornow, O., "CAA Broadband Noise Prediction for Aeroacoustic Design", Journal of Sound and Vibration 2011, doi:10.1016/j.jsv.2011.04.014.

[8]Ewert, R. and Neifeld, A., "A 3-D modal stochastic jet noise source model", 17th AIAA/CEAS Conference, Portland USA, 2011.

[9]Armstrong, R.R., Michalke, A. and Fuchs, H.V., "Coherent Structures in Jet Turbulence and Noise", AIAA Journal, Vol. 15, No. 7, July 1977.

[10]Michalke, A., "Some Remarks on Source Coherence Affecting Jet Noise", Journal of Sound and Vibration, Vol. 87(1), 1982.

[11]Morris, P.J., Boluriaan, S., "The prediction of jet noise from CFD data", AIAA/CEAS 10th Aeroacoustics Conference, 2004, AIAA Paper 2004-2977.

[12]Morris, P.J. and Farassat, F., "Acoustic Analogy and Alternative Theories for Jet Noise Prediction" AIAA Journal, Vol. 40, No. 4, April 2002.

[13]Morris, P.J. and Zaman, K.B.M.Q., "Two Component Velocity Correlations in Jets and Noise Source Modeling", AIAA/CEAS 10th Aeroacoustics Conference, 2010, AIAA Paper 2010-3781.

[14]Page, G.J., McGuirk, J.J., Hossain, M., Self, R.H. and Bassetti, A. "A CFD Coupled Acoustics Approach for Coaxial Jet Noise", AIAA/CEAS 9th Aeroacoustics Conference, 2003, AIAA Paper 2003-3286.

[15]Li, X.D., Schemel, C., Michel, U. and Thiele, F., "Azimuthal Sound Mode Propagation in Axisymmetric Duct Flows", AIAA Journal, Vol. 42, No. 10, 2004, pp. 2019-2027.

[16]Buske, C., Yu, C. and Zhuang, M., "Validation of a Zonal Approach Computing the Sound Radiation from Lined Ducts", AIAA Journal Vol. 48, No. 12, December 2010.

[17]Huang, X., Ma, Z., and Zhang, X., "Computation of Modal Radiation through an Engine Exhaust on Adaptively Refined Meshes", ECCOMAS CFD 2006.

[18]Zhang, X., Chen, X.X., Morfey, C.L. and Nelson, P.A., "Computation of Spinning Modal Radiation from an Unflanged Duct", AIAA Journal Vol. 42, No. 9, September 2004.

[19]Zhang, X., Chen, X.X. and Morfey, C.L., "Acoustic radiation from a semi-infinite duct with a subsonic jet", International Journal of Aeroacoustics Vol. 4, No. 1+2, 2005 pp.169-184.

[20]Bogey, C., Marsden, O. and Bailly, C., "Flow and acoustic fields of Reynolds number 10^5, subsonic jets with tripped exit boundary layers", AIAA 2010-3727

[21]Bogey, C. and Bailly, C., "Influence of the nozzle-exit boundary-layer thickness on the flow and acoustic fields of initially laminar jets", AIAA 2009-3409

[22]Grosche, F.-R., "Distributions of sound source intensities in subsonic and supersonic jets", AGARD-CP-131, 1974, pp. 4-1 to 4-10.

[23]Zaman, K.B.M.Q., "Effect of initial condition on subsonic jet noise", AIAA J., Vol.23, No. 9, 1985, pp.1370-1373.

[24]Zaman, K.B.M.Q., "Far-field noise of subsonic jet under controlled excitation", J. Fluid Mech., Vol. 152, 1985, pp. 83-111.